

# An open-source population balance modeling framework for the simulation of polydisperse multiphase flows

Ronald Lehnigk<sup>1</sup>  | William Bainbridge<sup>2</sup> | Yixiang Liao<sup>1</sup>  | Dirk Lucas<sup>1</sup>  |  
Timo Niemi<sup>3</sup> | Juho Peltola<sup>3</sup> | Fabian Schlegel<sup>1</sup> 

<sup>1</sup>Helmholtz-Zentrum Dresden – Rossendorf,  
Dresden, Germany

<sup>2</sup>CFD Direct Ltd, Reading, UK

<sup>3</sup>VTT Technical Research Center Ltd, Espoo,  
Finland

## Correspondence

Ronald Lehnigk, Helmholtz-Zentrum Dresden  
– Rossendorf, Bautzner Landstraße  
400, 01328 Dresden, Germany.  
Email: r.lehnigk@hzdr.de

## Funding information

Helmholtz European Partnering Program

## Abstract

Polydispersity is a challenging feature of many industrial and environmental multiphase flows, influencing all related transfer and transport processes. Besides their size, the fluid or solid particles may be distributed with respect to other properties such as their velocity or shape. Here, a population balance model based on the method of classes is combined with a multifluid solver within the open source computational fluid dynamics library OpenFOAM. The model allows for tracking the evolution of one or more size-conditioned secondary properties. It is applied to two different problems, the first being bubbly flow of air and water in a vertical pipe, where considering the velocity as a secondary property allows to resolve the size-dependent radial segregation. The second application is the gas phase synthesis of titania powder, where non-spherical particle aggregates appear whose shape is modeled through a collision diameter, leading to an improved prediction of the size distribution.

## KEYWORDS

Computational fluid dynamics (CFD), Method of classes, Multiphase flow, OpenFOAM, Population balance modeling

## 1 | INTRODUCTION

Polydisperse multiphase flows occur in a variety of industrial processes and are particularly relevant for power and process engineering. The defining characteristic is that the fluid or solid particles are countable and distributed with respect to various properties, first and foremost their size. Depending on the application, the distribution with respect to another variable such as velocity, shape, or chemical composition of the particles may have an influence on the process or the properties of the final product. The function characterizing the distribution is then referred to as bivariate or two-dimensional, whereas multivariate refers to a dependency on more than two properties. An example related to power engineering is the cocurrent flow

of a liquid and its vapor in a vertical pipe. Here, the developing radial phase distribution profile and by extension also the critical wall heat flux is governed mainly by non-drag forces such as shear-induced lift.<sup>1</sup> It strongly depends on the bubble size and can even change its direction, resulting in a separation of spherical and ellipsoidal bubbles.<sup>2</sup> Accordingly, the bubbles are distributed with respect to their size and velocity. An example from process engineering is the gas-phase synthesis of ceramic powders in flame reactors, for example for producing pigmentary titania, fumed silica, or alumina.<sup>3</sup> Following a reaction-driven nucleation, the morphology of the powder particles is largely determined by a competition between aggregation due to Brownian motion and high-temperature sintering.<sup>4</sup> Aggregation leads to the formation of particle clusters with a high specific

This is an open access article under the terms of the Creative Commons Attribution License, which permits use, distribution and reproduction in any medium, provided the original work is properly cited.

© 2021 The Authors. *AIChE Journal* published by Wiley Periodicals LLC on behalf of American Institute of Chemical Engineers.

surface area and a large collision cross section, which in turn increases the frequency of further collisions. Sintering on the other hand, that is, the coalescence of primary particles, makes the aggregates more compact. Essentially, the particle aggregates are distributed with respect to their volume and surface area, respectively their collisional diameter.

The development of property distributions can be tracked by solving a population balance equation.<sup>5,6</sup> Since about two decades, research is oriented toward its coupled solution with the governing equations of fluid flow within computational fluid dynamics (CFD) software, see for example References 7–9, with the primary aim to simulate the spatially heterogeneous evolution of size distributions or mean particle sizes. In this context, two commonly adopted approaches for solving the integro-partial differential population balance equation are the Quadrature-based method of moments (QMOM) and the method of classes.

In the QMOM, the population balance equation is rewritten as a set of transport equations for the lower order statistical moments of the size distribution function. Integral source terms are evaluated efficiently using Gaussian quadrature. Only a small number of scalar fields needs to be considered, making the approach attractive for implementation in CFD codes.<sup>10</sup> A disadvantage is that the distribution function is not directly accessible and must be reconstructed from the moments for validation against experimental data. Several variants of the QMOM exist, such as the Direct QMOM,<sup>11</sup> where the nodes and abscissas required from Gaussian quadrature are tracked directly, the Extended QMOM<sup>12</sup> that approximates the distribution function through a mixture of kernel density functions and the Conditional QMOM<sup>13</sup> which provides a moment inversion algorithm for multivariate distribution functions. An example from the literature where the spatial evolution of a bivariate distribution is modeled is the work of Zucca et al.,<sup>14</sup> who applied the Direct QMOM for simulating the formation of soot particles in turbulent combustion using the CFD code Fluent. Both the volume and the surface area were considered as distributed properties. Similarly, Buffo et al.<sup>15</sup> implemented the Conditional QMOM in the CFD code OpenFOAM to simulate a bubbly flow with mass transfer, taking the distribution with respect to size and chemical composition into account.

The method of classes approximates the distribution function through a discrete representation. Due to the larger number of required scalar fields, the computational cost tends to be greater compared to moment-based methods. Another limitation is the often very dominant error associated with the numerical approximation of growth or surface loss processes, for example, due phase or density changes. However, the distribution function is directly accessible such that the method of classes is particularly useful to validate and calibrate submodels for processes such as aggregation, coalescence or breakup. Various approaches to discretizing the integral source terms exist. In conjunction with CFD codes, the fixed pivot technique of Kumar and Ramkrishna<sup>16</sup> is used traditionally, for example, to simulate gas–liquid flows in bubble columns.<sup>8,17–20</sup> It allows to conserve up to two selected moments of the size distribution without introducing a constraint on the discretization. However, a drawback is the

circumstantial and inefficient treatment of binary bubble breakup models with an integrated or field-dependent daughter size distribution.<sup>21</sup> Another prominent class method variant is the Multiple Size Group (MUSIG) model of Lo<sup>22</sup> due to its availability in the commercial code CFX. It found application for the simulation of two-phase flows in vertical pipes<sup>23–26</sup> as well as bubble column reactors.<sup>27,28</sup> The associated breakup scheme is specifically intended for binary breakup models with an integrated and field-dependent daughter size distribution. However, Liao et al.<sup>21</sup> showed that the MUSIG model is non-conservative with respect to the total particle number. Depending on the discretization, breakup can be severely overestimated, making it unsuitable for a reliable calibration of submodels. Tracking the spatial evolution of a bivariate distribution function by discretizing it along both property coordinates is associated with a large computational effort. A compromise is to not resolve the distribution function along the second coordinate, but to compute size-conditioned averages. This means for example that locally, all particles of a given size share the same velocity or surface area. In this manner, Bhole et al.<sup>8</sup> consider separate velocities for each bubble size class using an algebraic slip approach. Jeong et al.<sup>29</sup> track both the volume and surface area concentration in a simulation of non-spherical polydisperse particle growth. Similarly, Krepper et al.<sup>30</sup> adopt the inhomogeneous MUSIG model<sup>31</sup> that allows to compute an individual velocity field for a specified range of bubble sizes by considering a complete gas phase momentum balance. Note that the aforementioned inconsistency of the MUSIG model is inherited.

The objective of this work is to develop a flexible, robust, and well-verified tool for the multidimensional numerical simulation of polydisperse multiphase flows where processes such as aggregation, coalescence, and breakup dominate the evolution of the size distribution. To this end, a population balance model based on the method of classes is combined with an Eulerian multifluid solver within the open source CFD library OpenFOAM. While implementations of the method of classes in OpenFOAM have been reported before,<sup>18,19,32,33</sup> this is the first development that is directly included in the OpenFOAM Foundation release, thereby ensuring unrestricted accessibility and long-term availability. The framework itself is novel in two aspects. First, it is flexible in terms of the breakup models that can be applied. Models based on a total breakup frequency and a separate daughter size distribution as well as binary breakup models with an integrated daughter size distribution are supported, while the particle number and mass is consistently preserved, irrespective of how the size domain is discretized. Second, a general formulation that allows to consider an arbitrary number of secondary average particle properties is presented, either conditioned on each size class or a consecutive ensemble of size classes. To demonstrate the versatility of the tool, it is applied to two fundamentally different problems from power and process engineering. First, simulations of the cocurrent flow of air and water in a vertical pipe are carried out with particular emphasis on the size dependency of the bubble velocity. Second, the gas phase synthesis of titania powder in a laboratory aerosol reactor is simulated, where the focus lies on modeling the shape of the non-spherical particle aggregates synthesized in the reactor. All test and simulation setups are available together with this article.

## 2 | METHOD

### 2.1 | Population balance model

For ease of notation, the simplified case with particle size as the only distributed property is considered first. Formulated in terms of a transport equation for the univariate volume-based number density function  $n_v$ , the population balance equation states

$$\frac{\partial n_v}{\partial t} + \nabla \cdot (\vec{u} n_v) = h_v. \quad (1)$$

Thereby, the particles are assumed to share a single velocity field  $\vec{u}$ , which is only acceptable if their inertia is small, if collisions are not important, and if the size distribution is sufficiently narrow such that the size dependency of interfacial forces has a weak influence. In addition, the particles are assumed to be spherical at this point. As highlighted in Section 1, these assumptions may be inappropriate and are relaxed later by introducing an approach for considering secondary particles properties, see Section 2.1.2. Continuing with the univariate case, the source term of Equation (1) states:

$$h_v = \frac{1}{2} \int_0^v n_{v'} n_{v-v'} \tilde{C}_{v',v-v'} dv' - n_v \int_0^\infty n_{v'} \tilde{C}_{v,v'} dv' + \int_v^\infty n_{v'} \tilde{B}_{v'} \beta_{v,v'} dv' - n_v \tilde{B}_v - \frac{\partial(\dot{v}_v n_v)}{\partial v} + \dot{n}_v. \quad (2)$$

Birth and death by coalescence or aggregation are represented by the first two terms on the right hand side of Equation (2), where  $\tilde{C}_{v,v'}$  is the corresponding frequency. The third and fourth term on the right hand side describe birth and death by breakup, where  $\tilde{B}_{v'}$  is the total breakup frequency. Information about the number and distribution of the daughter particles is provided through the daughter size distribution function  $\beta_{v,v'}$  which must satisfy the following constraints:

$$\int_0^{v'} v \beta_{v,v'} dv = v', \quad (3)$$

$$\int_0^{v'} \beta_{v,v'} dv = \gamma. \quad (4)$$

Here,  $\gamma$  is the total number of daughter particles born from the breakup event. The fifth term on the right hand side of Equation (2) is relevant during density or phase change processes, where  $\dot{v}_v$  is the drift rate which describes the change in particle volume. Phase change processes also lead to the nucleation or disappearance of particles, which is covered by the last term in Equation (2).

In the present work, Equation (1) is solved by discretizing the size domain into a set of classes with lower and upper boundaries  $v_i$  and  $v_{i+1}$ .

An integration of the number density function over the resulting intervals yields the number concentration

$$N_i = \int_{v_i}^{v_{i+1}} n_v dv \quad (5)$$

of particles in each class, for which a separate transport equation is solved:

$$\frac{\partial N_i}{\partial t} + \nabla \cdot (\vec{u} N_i) = H_i. \quad (6)$$

The discrete source term  $H_i$  in Equation (6) is approximated using the established formulation of Kumar and Ramkrishna.<sup>16</sup> It assumes that the population is concentrated at the so-called pivotal volumes  $x_i$  and applies the mean value theorem on the frequencies. The technique conserves two selected moments of the distribution without introducing any constraint on the discretization. Coalescence, breakup, or nucleation events leading to a non-pivotal contribution are handled by distributing the number gain between the nearby classes  $x_i \leq v \leq x_{i+1}$ . Note that the method can also be extended to conserve an arbitrary number of moments, including monovariate<sup>34</sup> as well as bi- and multivariate population balances.<sup>35,36</sup>

**Coalescence and breakup:** Excluding drift and nucleation, the discrete source term states

$$H_i|_{\text{coalescence, breakup}} = \sum_{j=0}^i N_j \sum_{k=j}^i \left(1 - \frac{1}{2} \delta_{jk}\right) \eta_{x_j+x_k} N_k \tilde{C}_{jk} - N_i \sum_{j=0}^M N_j \tilde{C}_{ij} + \sum_{j=i}^M N_j \tilde{B}_j n_{ij} - N_i \tilde{B}_i, \quad (7)$$

where the Kronecker's delta  $\delta_{jk}$  prevents double-counting of coalescence events. The number and mass conservative distribution in case of non-pivotal events is ensured by

$$\eta_v = \begin{cases} \frac{v - x_{i-1}}{x_i - x_{i-1}} & \text{if } x_{i-1} \leq v \leq x_i, \\ \frac{x_{i+1} - v}{x_{i+1} - x_i} & \text{if } x_i < v \leq x_{i+1}, \\ 0 & \text{else} \end{cases} \quad (8)$$

and

$$n_{ij} = \int_{x_i}^{x_{i+1}} \frac{x_{i+1} - v}{x_{i+1} - x_i} \beta(v, x_j) dv + \int_{x_{i-1}}^{x_i} \frac{v - x_{i-1}}{x_i - x_{i-1}} \beta(v, x_j) dv. \quad (9)$$

Note that Equations (8) and (9) can be formulated such that any two moments of the distribution are conserved. From the number concentration in a class, an approximate value of the number density can be obtained by

$$n_v(x_i) = \frac{N_i}{v_{i+1} - v_i}. \quad (10)$$

The section boundaries  $v_i$  are defined to lie halfway between the pivots, that is,  $v_i = (x_i + x_{i-1})/2$ .

**Nucleation:** The nucleation term describes the birth of particles at the lower end of the size range due to phase change. In the discrete formulation, the corresponding source term states

$$H_i|_{\text{nucleation}} = \frac{\dot{m}_{dc} \eta_{v_{\text{nuc}}}}{x_i \rho_d}, \quad (11)$$

where  $\rho_d$  is the density of the dispersed phase and  $\dot{m}_{dc}$  the mass transfer rate per unit volume between the continuous phase  $c$  and the dispersed phase  $d$ . To ensure mass and number conservation in the event that the nucleus volume  $v_{\text{nuc}}$  does not match a pivotal volume, the number gain is again distributed using Equation (8). Note that number and mass conservation also requires that the representative volume of the first size class is equal to or smaller than the nucleus volume, that is,  $x_0 \leq v_{\text{nuc}}$ .

**Drift:** The treatment of the drift term, which describes the convection of the number density function along the size coordinate, is particularly problematic for any class method approach with fixed boundaries. Cases that are dominated by drift should be analyzed carefully with respect to the error introduced as a result of the numerical approximation. An ideal scheme can be used on any kind of grid and conserves at least the total number and mass of particles while reducing numerical diffusion without causing oscillations. Kumar<sup>37</sup> applied several approximations of the drift term to the classical problem of a block profile transport. The scheme of Hounslow et al.<sup>38</sup> was shown to introduce oscillations and negative values that must be set to zero, causing a violation of the number and mass conservation. Oscillations also occur with the scheme of Park and Rogak,<sup>39</sup> albeit numbers and mass are properly conserved. A promising alternative that could be considered for future developments is presented by Cheng et al.,<sup>40</sup> who adopted the scheme of Kurganov and Tadmor<sup>41</sup> and present it in a form that can be used on geometric grids. It is free from oscillations and leads to reduced numerical diffusion for the test case of Kumar,<sup>37</sup> but it remains unclear whether numbers and mass are always conserved.

In this work, an upwind formulation is employed to avoid oscillations or unboundedness of the size class fractions. The scheme conserves numbers and mass on any type of grid resulting in a stable computation of the drift-induced mass transfer between velocity groups. The numerical diffusion of the number density function is accepted, because the term is only relevant for the simulation of the gas-liquid flow presented in Section 3, for which coalescence and breakup dominate. The discrete approximation of the drift term states

$$H_i|_{\text{drift}} = w_i \frac{\dot{x}_{i-1} N_{i-1}}{x_i - x_{i-1}} - p_i \dot{x}_i N_i + e_i \frac{\dot{x}_{i+1} N_{i+1}}{x_i - x_{i+1}}, \quad (12)$$

where  $\dot{x}_i$  is the drift rate evaluated for the pivotal volume and

$$w_i = \begin{cases} 1 & \text{if } \dot{x}_{i-1} > 0 \text{ and } i > 0, \\ 0 & \text{else,} \end{cases} \quad (13)$$

$$p_i = \begin{cases} (x_{i+1} - x_i)^{-1} & \text{if } \dot{x}_i > 0 \text{ and } i < M, \\ (x_{i-1} - x_i)^{-1} & \text{if } \dot{x}_i < 0 \text{ and } i > 0, \\ 0 & \text{else,} \end{cases} \quad (14)$$

$$e_i = \begin{cases} 1 & \text{if } \dot{x}_{i+1} < 0 \text{ and } i < M, \\ 0 & \text{else.} \end{cases} \quad (15)$$

### 2.1.1 | An alternative treatment for binary breakup

As highlighted by Liao et al.,<sup>21</sup> the discrete breakup formulation of Kumar and Ramkrishna<sup>16</sup> is efficient when the daughter size distribution does not depend on field parameters. The results of Equation (9) can then be tabulated for all mother and daughter combinations at the beginning of a simulation. Ideally, the model allows for an analytical solution of the integrals. The cost increases substantially when the daughter size distribution is field-dependent. It is increased further if the daughter size distribution is given implicitly as in the models of Luo and Svendsen<sup>42</sup> or Liao et al.,<sup>26</sup> which provide an expression for the partial breakup frequency

$$\tilde{B}_{v,v'} = \tilde{B}_v \beta_{v,v'}. \quad (16)$$

To apply the approach of Kumar and Ramkrishna,<sup>16</sup> the total breakup frequency and the daughter size distribution needs to be extracted from Equation (16). To this end, the total breakup frequency must be computed for every mother size and control volume by

$$\tilde{B}_v = \frac{1}{2} \int_0^v \tilde{B}_{v,v'} dv' \quad (17)$$

as done for example by Bannari et al.<sup>18</sup> Furthermore, volume-averaged input parameters are sometimes used in the daughter size distribution to bring the cost to an acceptable level.<sup>20</sup> Simply inserting the partial breakup frequency into the population balance equation and discretizing it implies an application of the mean value theorem on the daughter size distribution. The MUSIG model of Lo<sup>22</sup> follows this strategy which leads to number conservation issues on non-uniform grids. An alternative solution is to resort to a certain discretization pattern, for example, using the formulation of Hagesaether et al.,<sup>43</sup> which constitutes a loss of flexibility. In this work, the formulation of Liao et al.<sup>21</sup> is applied which relies on the symmetry of the daughter size distribution in case of binary breakup and does not exhibit any of the above disadvantages. The corresponding source term states

$$H_i = \sum_{j=i}^M N_j \left( \tilde{B}_{ij} \Delta v_i(j) + \sum_{k=0}^j \tilde{B}_{kj} \eta_{x_j - x_k} \Delta v_k(j) \right) - N_i \sum_{j=0}^i \tilde{B}_{ji} \Delta v_j(i). \quad (18)$$

The first part in the birth term describes all pivotal contributions to class  $i$ . The second summation within the birth term accounts for the possibility that a binary breakup event, defined through the pivotal volumes  $x_j$  and  $x_k$ , contributes to class  $i$  by producing a counterpart with volume  $v = x_j - x_k$  that falls into the range of  $x_{i-1} < v < x_{i+1}$ . A number and mass conservative distribution of the number gain among the neighboring classes is ensured by using the weight function  $\eta_v$ , Equation (8). The section widths

$$\Delta v_i(j) = \begin{cases} v_{i+1} - v_i & \text{if } v_{i+1} \leq x_j/2, \\ x_j/2 - v_i & \text{if } v_i < x_j/2 < v_{i+1}, \\ 0 & \text{if } v_i \geq x_j/2 \end{cases} \quad (19)$$

are a function of the mother class  $j$ , acknowledging the symmetry of the daughter size distribution. Note that Equation (18) can also be used in combination with models that state a total breakup rate together with a binary but field-dependent daughter size distribution function, simply by substituting

$$\tilde{B}_{ij} = \tilde{B}_j \beta(x_i, x_j) \quad (20)$$

into Equation (18).

### 2.1.2 | Tracking secondary particle properties

As discussed in Section 1, the distribution of the dispersed phase particles with respect to other properties can be relevant. In case of two properties, the number density function  $n_{\vec{\xi}}$  is referred to as bivariate and the internal state is described by the vector  $\vec{\xi} = (\xi_1, \xi_2)^T$ . Here, the size distribution of the particles is of key interest and therefore the particle volume  $v$  is selected as the primary internal coordinate  $\xi_1$ . The secondary internal coordinate  $\xi_2$  is chosen depending on the application. In order to track the development of a distribution with respect to two properties, the bivariate population balance equation could be discretized along both coordinates, which leads to a total of  $M_v \times M_{\xi_2}$  classes. However, the computational expense associated with solving a bivariate population balance equation with the method of classes is quite large and unsuitable for the solution of spatially inhomogeneous problems. As a trade-off between accuracy and computational effort, only the number-weighted mean value of the secondary property for a given pivotal volume  $x_i$  is considered here. It is tracked as an additional representative property of each class. Given a bivariate number density function  $n_{v,\xi_2}$ , it can be computed by

$$\bar{\xi}_{2,i} = \left( \int_{-\infty}^{\infty} d\xi_2 \int_{v_i}^{v_{i+1}} dv [\xi_2 n_{v,\xi_2}] \right) \left( \int_{-\infty}^{\infty} d\xi_2 \int_{v_i}^{v_{i+1}} dv [n_{v,\xi_2}] \right)^{-1} \quad (21)$$

While the representative volume assigned to each class is fixed,  $\bar{\xi}_{2,i}$  constitutes a variable particle property for which an additional

transport equation is solved. In the corresponding transport equation, interactions between the classes then need to be considered by adding the following source terms

$$\begin{aligned} H_{\bar{\xi}_{2,i}} = & \sum_{j=0}^i N_j \sum_{k=j}^i \frac{\bar{\xi}_{2,j} x_j + \bar{\xi}_{2,k} x_k}{x_j + x_k} \left( 1 - \frac{1}{2} \delta_{jk} \right) \eta_v N_k \tilde{C}_{jk} - \bar{\xi}_{2,i} N_i \sum_{j=0}^M N_j \tilde{C}_{ij} \\ & + \sum_{j=i}^M \bar{\xi}_{2,j} N_j \tilde{B}_{ij} \eta_{ij} - \bar{\xi}_{2,i} N_i \tilde{B}_i \\ & + \bar{\xi}_{2,i-1} w_i \frac{\dot{x}_{i-1} N_{i-1}}{x_i - x_{i-1}} - \bar{\xi}_{2,i} \frac{\dot{x}_i N_i}{x_{i+1} - x_i} + \bar{\xi}_{2,i+1} e_i \frac{\dot{x}_{i+1} N_{i+1}}{x_i - x_{i+1}} + S_{\bar{\xi}_{2,i},nuc} \end{aligned} \quad (22)$$

Nucleation left aside, these terms describe the number-weighted exchange of the secondary property between the size classes assuming that it is conserved. The nucleation term

$$S_{\bar{\xi}_{2,i},nuc} = \bar{\xi}_{2,i,nuc} \frac{\dot{m}_{dc} \eta_{v,nuc}}{x_i \rho_d} \quad (23)$$

requires a birth value for  $\bar{\xi}_{2,i,nuc}$  to be specified or modeled. The terms in Equation (22) are almost identical to those in Equation (7), apart from the additional multiplication with the secondary property values of the original classes. When the alternative formulation for binary breakup presented in Section 2.1.1 is used, the corresponding source terms in the transport equation for  $\bar{\xi}_{2,i}$  states

$$H_{\bar{\xi}_{2,i}} = \sum_{j=i}^M N_j \left( \bar{\xi}_{2,j} \tilde{B}_{ij} \Delta v_i(j) + \sum_{k=0}^j \bar{\xi}_{2,k} \tilde{B}_{kj} \eta_v \Delta v_k(j) \right) - \bar{\xi}_{2,i} N_i \sum_{j=0}^i \tilde{B}_{ji} \Delta v_j(i). \quad (24)$$

Instead of assigning a separate secondary property field to each class, it can also be shared by an ensemble of consecutive classes. In the case of such a lumped treatment, the source term contributions for several combinations of classes in Equation (22) cancel out since only interactions across ensemble boundaries have a net effect. The corresponding source term in the transport equation for the ensemble averaged secondary property then states

$$H_{\bar{\xi}_{2,\varphi}} = \sum_{\psi=0, \psi \neq \varphi}^N \left( S_{\bar{\xi}_{2,\varphi\psi}} - S_{\bar{\xi}_{2,\psi\varphi}} \right), \quad (25)$$

wherein  $\varphi$  represents the index and

$$N_{\varphi} = \sum_{i \in \varphi} N_i \quad (26)$$

the particle number concentration of the ensemble. The rate of exchange due to interactions with another ensemble  $\psi$  is then given by

$$S_{\bar{\xi}_{2,\psi}} = \bar{\xi}_{2,\psi} \sum_{i \in \psi} \left[ \sum_{j=0}^i N_j \sum_{k=j}^i \frac{x_j}{x_j + x_k} \left(1 - \frac{1}{2} \delta_{jk}\right) \eta_v N_k \tilde{C}_{jk} \right. \\ \left. + \sum_{j=0}^i N_j \sum_{k=j}^i \frac{x_k}{x_j + x_k} \left(1 - \frac{1}{2} \delta_{jk}\right) \eta_v N_k \tilde{C}_{jk} \right. \\ \left. + \sum_{j=i}^M \tilde{N}_j \tilde{B}_{ij} \eta_{ij} + w_i \underbrace{\frac{\dot{x}_{i-1} N_{i-1}}{x_i - x_{i-1}}}_{\text{if } i-1 \in \psi} + e_i \underbrace{\frac{\dot{x}_{i+1} N_{i+1}}{x_i - x_{i+1}}}_{\text{if } i+1 \in \psi} \right] \quad (27)$$

and, when the alternative breakup formulation is used, by

$$S_{\bar{\xi}_{2,\psi}} = \bar{\xi}_{2,\psi} \sum_{i \in \psi} \left[ \sum_{j=i,j \in \psi}^M N_j \tilde{B}_{ij} \Delta v_i(j) + \sum_{j=i}^M N_j \sum_{k=0,k \in \psi}^j \tilde{B}_{kj} \eta_v \Delta v_k(j) \right]. \quad (28)$$

Equations (27) and (28) only include birth events, hence  $S_{\bar{\xi}_{2,\psi}} \geq 0$ . The corresponding death terms do not need to be tracked separately. They are accounted for by  $S_{\bar{\xi}_{2,\psi}}$  in Equation (25), which represents the sum of all birth events in the ensemble  $\psi$  due to interactions with another ensemble  $\varphi$ .

## 2.2 | Implementation in an Eulerian multifluid solver

The population balance model is implemented within the open source CFD library OpenFOAM and combined with an Eulerian multifluid solver. The solver is capable of handling an arbitrary number of compressible phases. Following the idea of the two-fluid model of Ishii,<sup>44</sup> the transfer of mass, momentum, and energy between the phases is entirely modeled. A derivation of the corresponding continuity and momentum equations by means of conditional density-weighted ensemble averaging is presented by Weller.<sup>45</sup>

### 2.2.1 | Substitution of the solution variable

The pivotal volumes  $x_i$  are fixed in space and time such that the number concentrations  $N_i$  can be expressed in terms of the volume concentrations

$$\alpha_i = x_i N_i. \quad (29)$$

The sum of these volume concentrations represents the phase fraction  $\alpha$  of the dispersed phase, such that the solution of a continuity equation for the dispersed phase is actually a redundant step. However, the solver relies on a multidimensional flux-limiting

technique for the explicit solution of the continuity equations, which successfully mitigates transport-induced mass conservation errors and keeps the phase fractions bounded.<sup>46</sup> With the phase fractions already solved for, the task of the population balance model is to determine how the given dispersed phase mass is distributed with respect to size. The model solves for the size class fractions

$$f_i = \frac{\alpha_i}{\alpha_d}, \quad (30)$$

which are bounded between zero and one and should sum to unity. Slight violations can be handled by scaling each size class fraction based on the sum of all size class fractions:

$$f_i^{\text{new}} = \frac{f_i^{\text{old}}}{\sum_i f_i^{\text{old}}}. \quad (31)$$

With the size class fractions as solution variables, the number concentrations in the former equations are substituted by

$$N_i = \frac{f_i \alpha_d}{x_i}. \quad (32)$$

### 2.2.2 | Velocity group concept

In Section 2.1.2, a general strategy for handling a secondary internal coordinate within the population balance model was presented. The dispersed phase velocity constitutes a useful choice of such a coordinate. Ideally, a velocity field should be computed for each size class in order to resolve the size dependency of the dispersed phase motion. To keep the computational expense at an acceptable level, the lumped treatment presented in Section 2.1.2 is adopted here, whereby sets of consecutive size classes are combined into the so-called velocity groups, analogous to the inhomogeneous MUSIG approach described by Krepper et al.<sup>30</sup> An individual continuity and momentum equation is solved for each velocity group, wherein all possible exchange processes with the continuous phase are taken into account. Transfers of momentum between the velocity groups resulting from coalescence, breakup or drift are also accounted for. In the computational sense, the velocity groups are treated as separate phases. In the physical sense however, they are representatives of the dispersed phase and share a common set of thermo-physical properties.

*Continuity equation:* The continuity equation for phase  $\varphi$  states

$$\frac{\partial(\alpha_\varphi \rho_\varphi)}{\partial t} + \nabla \cdot (\alpha_\varphi \rho_\varphi \vec{u}_\varphi) = S_{\alpha,\varphi}, \quad (33)$$

wherein  $S_{\alpha,\varphi}$  represents all mass sources and mass transfer terms. By introducing velocity groups, it is useful to redefine the size class fractions on a per-phase basis, that is,



$$f_{i,\varphi} = \frac{f_i \alpha_d}{\alpha_\varphi}, \quad (34)$$

wherein

$$\alpha_d = \sum_{\varphi \in d} \alpha_\varphi \quad (35)$$

is the total dispersed phase fraction and

$$\sum_{i \in \varphi} f_{i,\varphi} = 1 \quad (36)$$

for each velocity group. Following this definition,  $f_i \alpha$  is replaced by  $f_{i,\varphi} \alpha_\varphi$  in Equation (32). The source term

$$S_{\alpha,\varphi} = \dot{m}_\varphi + \sum_{\psi=0, \psi \neq \varphi}^N (\dot{m}_{\varphi\psi} - \dot{m}_{\psi\varphi}) \quad (37)$$

gives the net rate of change of the mass of phase  $\varphi$  in the system, where  $\dot{m}_{\varphi\psi}$  is the positive mass transfer rate from phase  $\varphi$  to phase  $\psi$ . Injections of mass within the computational domain are considered through  $\dot{m}_\varphi$ . Interfacial mass transfers such as a reaction-driven phase change on the other hand are represented by  $\dot{m}_{\varphi\psi}$ , causing a source in phase  $\varphi$  and a sink in phase  $\psi$ . When using velocity groups, the mass transfer due to coalescence, breakup, and drift needs to be considered. The associated mass transfer rate is obtained from Equation (25), wherein  $\bar{\varepsilon}_2$  is substituted by the density of the corresponding velocity group.

**Momentum equation:** The momentum equation for phase  $\varphi$  states

$$\frac{\partial (\alpha_\varphi \rho_\varphi \vec{u}_\varphi)}{\partial t} + \nabla \cdot (\alpha_\varphi \rho_\varphi \vec{u}_\varphi \vec{u}_\varphi) - \nabla \cdot \tau_\varphi = -\alpha_\varphi \nabla p + \alpha_\varphi \rho_\varphi \vec{g} + \mathbf{M}_\varphi + \mathbf{S}_{M,\varphi}, \quad (38)$$

where  $p$  is the shared pressure and  $\vec{g}$  the gravitational acceleration. If the motion of the phase is turbulent, the corresponding momentum equation may be considered as Reynolds-averaged. In that case, the shear stress tensor  $\tau_\varphi$  also includes the Reynolds stresses which need to be modeled accordingly. Also, when describing the collision-dominated motion of solid particles, the stress tensor may be modeled using the kinetic theory of granular flows.<sup>47–49</sup> The rate of interfacial momentum transfer  $\mathbf{M}_\varphi$  requires modeling as well, including the effects of drag and possibly contributions from virtual mass, turbulent dispersion, and lift forces. It is a function of the Sauter mean diameter which is calculated from

$$d_{32,\varphi} = 6 \left( \sum_i \frac{a_i f_{i,\varphi}}{x_i} \right)^{-1}, \quad (39)$$

where  $a_i$  is the representative surface area of the particles in each size class. In the case of spherical particles, the expression simplifies to

$$d_{32,\varphi} = \left( \sum_i \frac{f_{i,\varphi}}{d_i} \right)^{-1}. \quad (40)$$

When the dispersed phase is split into velocity groups, the corresponding overall Sauter mean diameter is obtained from

$$d_{32} = \left( \sum_{\varphi \in d} \frac{\alpha_\varphi}{d_{32,\varphi}} \right)^{-1}. \quad (41)$$

Further momentum sources are accounted for in Equation (38) by

$$\mathbf{S}_{M,\varphi} = \mathbf{F}_\varphi + \dot{m}_\varphi \vec{u} + \sum_{\psi=0, \psi \neq \varphi}^N (\dot{m}_{\varphi\psi} \vec{u}_\psi - \dot{m}_{\psi\varphi} \vec{u}_\varphi), \quad (42)$$

where  $\mathbf{F}_\varphi$  represents additional volume forces acting on phase  $\varphi$  within the domain. Momentum is also created by the injection of mass within the computational domain, which is covered by the second term. The third term represents the momentum transfer due to interfacial mass transfers. This includes the artificial mass transfer between velocity groups due to coalescence, breakup, and drift.

The implementation of the population balance model in the multifluid solver was thoroughly verified. An overview of the solution procedure for the equations presented above and results for various test cases are provided as Supplementary Material.

### 3 | COCURRENT FLOW OF AIR AND WATER IN A VERTICAL PIPE

In the following, the application of the model on a cocurrent flow of air and water in a vertical pipe with an inner radius of 25.6 mm and a length of 3 m is presented. The bubble velocity is introduced as a secondary property by adopting the velocity group concept described in Section 2.2.2, a variant of the lumped secondary property treatment presented in Section 2.1.2. This allows to reproduce a possible radial separation of bubbles according to their size, mainly resulting from shear-induced lift. Under normal temperature and pressure conditions, the investigated air and water superficial velocities are 0.219 and 1.611 ms<sup>-1</sup> respectively. The data used for validation originates from the experiment of Lucas et al.,<sup>50</sup> who applied wire mesh sensors for measuring the velocity and volume fraction of the gas-phase as well as the bubble size distribution.

#### 3.1 | Computational domain and boundary conditions

The largely axisymmetric nature of the flow observed in the experiment allows for a two-dimensional computational domain. In the radial direction, it is subdivided into 50 cells. The cell width decreases

linearly toward the wall with a ratio of 0.375 between the first and the last cell.<sup>51</sup> In the axial direction, a grid spacing of 5 mm is adopted. The experiment features a sparger device consisting of a system of 19 needles that are distributed uniformly over the pipe cross section. In the simulation, it is represented approximately through a radially uniform mass source that extends from a length to diameter ratio  $L/D = 0$  to 0.6. The corresponding bubble size distribution is based on the integral size distribution measured at  $L/D = 0.6$ . At the inlet, the water velocity is set to a value of  $1.611 \text{ ms}^{-1}$ , equivalent to the water superficial velocity. In order to ensure that the water velocity profile is fully developed prior to the point of injection, the computational domain is extruded in the upstream direction by 0.2 m. At a domain length of 0.1 m, the computed velocity, turbulent kinetic energy, and eddy frequency profiles are extracted and mapped back to the inlet. The resulting velocity profile is then scaled in order to retain the correct average water flow rate. At the wall, a slip condition is used for the air phase and a no-slip condition for the water phase. All mass exits at the top of the domain where the pressure is set to  $1.139 \times 10^5 \text{ Pa}$ . Both air and water have a temperature of  $30^\circ\text{C}$ .

### 3.2 | Key modeling aspects

The interfacial exchange of momentum is modeled using the combination of closure relations recommended by Liao et al.,<sup>52</sup> which includes the lift force coefficient model of Tomiyama et al.<sup>2</sup> Turbulence is modeled using the  $k-\omega$  based shear stress transport model of Menter and Esch,<sup>53</sup> in combination with the bubble-induced turbulence model of Ma et al.<sup>54</sup> and the blended wall function treatment of Rzehak and Kriebitzsch.<sup>51</sup> Coalescence and breakup frequencies are computed using the model of Lehr et al.<sup>7</sup> Two simulations are performed. In the first, denoted as 1VG, all bubbles are assumed to share a single velocity field while for the second, denoted as 4VG, the size distribution is split into four velocity groups according to the turning points of the lift force coefficient model, that is, at  $d = 4.4, 5.8$ , and 7 mm. In both cases, the size distribution is approximated by 18 size classes, using a section spacing of  $\Delta d = 1 \text{ mm}$ .

### 3.3 | Results and discussion

Figure 1A shows the radial air phase fraction profile at different axial positions. In the experiment, it initially features a peak near the wall. The profile gradually becomes core-peaked as the flow develops, while a second less dominant local maximum remains near the wall. This evolution is characteristic for a transition from bubbly to near-slug flow conditions. As described by Lucas et al.,<sup>55</sup> small spherical bubbles first migrate toward the wall after their injection due to shear-induced lift. Here, the increased bubble number concentration leads to coalescence. Once the bubbles are large enough to deform, the direction of the lift force changes and they tend to migrate toward the pipe center. Figure 1B presents the size-specific phase fraction profiles at the highest measurement level. It shows that spherical

bubbles with a size smaller than 5.8 mm occur mainly near the wall while larger bubbles are found predominantly in the pipe center. Thus, the experimental data supports the applicability of the lift force model of Tomiyama et al.<sup>2</sup>

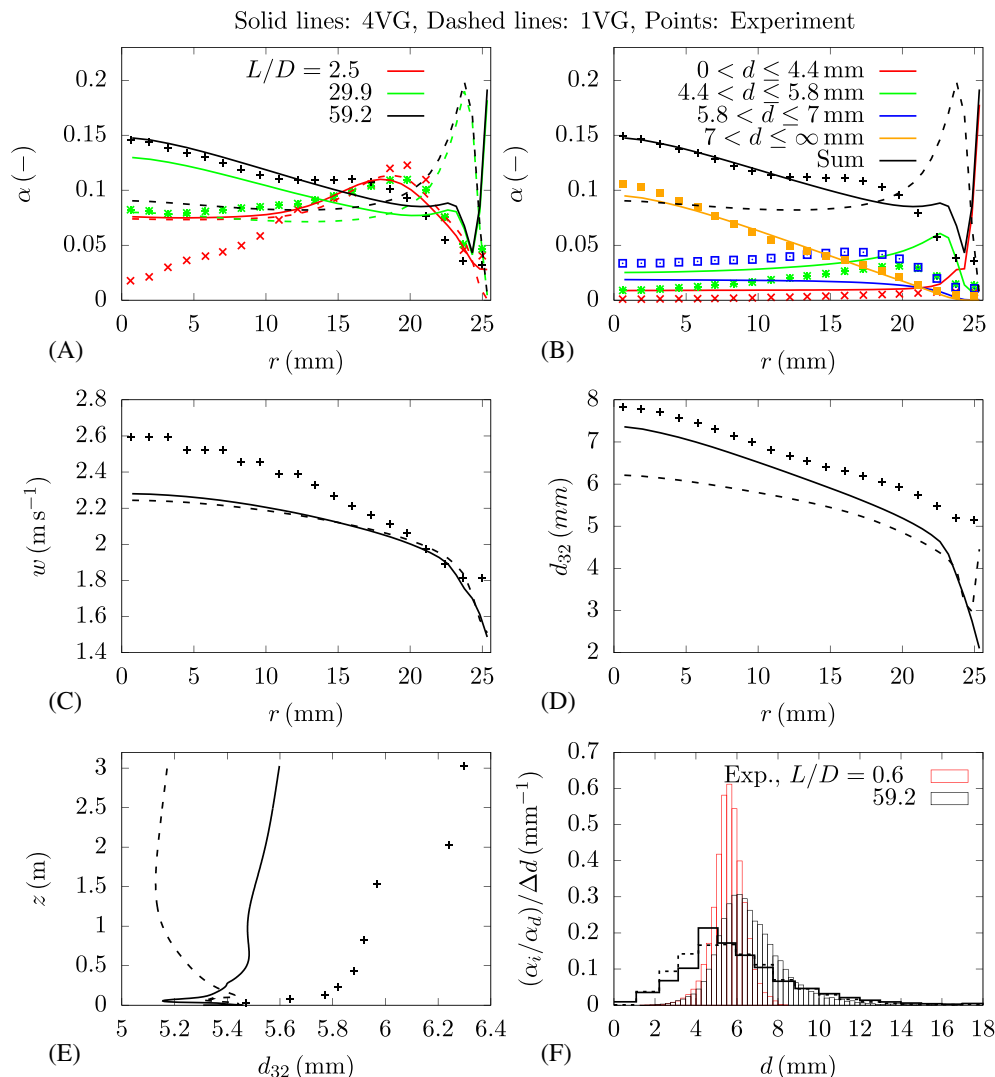
While there is room for improvement in quantitative terms, the simulation based on four velocity groups reproduces the transition process (Figure 1A) as well as the size-dependent radial separation (Figure 1B) quite well. At  $L/D = 59.2$ , the agreement with the experiment is particularly good for the core region where bubbles larger than 7 mm dominate. As in the experiment, the simulated phase fraction profile also exhibits a second local maximum, albeit it is located too close to the wall. Directly at the wall, a third peak is predicted. Whether this peak is present in the experiment as well is unclear, because the wire mesh sensor resolution leaves bubbles smaller than 2 mm undetected. However, the work of Zaruba et al.<sup>56</sup> suggests that smaller bubbles could slide along the wall.

When simulating the flow with a single velocity group on the other hand, the flow remains wall-peaked toward the end of the domain (Figure 1A). This can be attributed to the missing degree of freedom that allows for a size-dependent separation of bubbles at the control volume level. With one velocity group, the direction and magnitude of the lift force vector is determined for the entire bubble ensemble, whereby a local separation is suppressed. For the case with four velocity groups, the size classes are distributed such that the size distribution within a velocity group only determines the magnitude of the lift force, but not its direction. The differences in the results are expected to increase as the predicted local bubble size distribution becomes wider and extends across lift force regimes.

In terms of the air velocity profile predicted at the end of the domain, Figure 1C, the differences between both approaches are negligible. The agreement is best for the near-wall region and the deviation increases gradually toward the pipe center. The differences with respect to the radial and axial Sauter mean diameter profiles (Figure 1D,E) are again more pronounced. The simulation results are generally closer to the experiment when using four velocity groups. Figure 1F presents the measured integral size distribution at the bottom and top of the domain. Coalescence and bubble growth clearly dominate in the experiment, such that the size distribution becomes wider as the flow develops. The predicted size distribution at  $L/D = 59.2$  agrees best for its tail, that is, for bubbles larger than 9 mm. For bubbles with a size of 5–9 mm, the volume concentration is underestimated. On the other hand, it is overestimated for smaller bubbles. The discrepancies are consistent with those observed for the size-specific phase fraction profiles (Figure 1B). Thus, an improved modeling of coalescence and breakup is expected to immediately improve the prediction of the radial profiles. The size distribution predicted with one velocity group differs only slightly from those obtained with four velocity groups and is most pronounced for bubbles with a size smaller than about 5 mm. It should be noted however that only the integral distribution is presented here. Differences for the local size distribution are again more pronounced, which can also be concluded from differences between the predicted radial profiles of the Sauter mean diameter (Figure 1D).



**FIGURE 1** Results for simulation of cocurrent flow of air and water using one (1VG) and four velocity groups (4VG). (A) Radial air phase fraction profiles for various axial positions (in terms of the length to diameter ratio  $L/D$ ); (B) integral and size-specific radial air phase fraction profiles at  $L/D = 59.2$ ; (C) radial air velocity profile at  $L/D = 59.2$ ; (D, E) radial ( $L/D = 59.2$ ) and axial Sauter mean diameter profile; and (F) integral size distribution



While splitting the size distribution into velocity groups was shown to improve the simulation results for the presented case, it is also associated with an additional cost. An evaluation of the computational performance is provided as Supplementary Material.

## 4 | VAPOR SYNTHESIS OF TITANIA POWDER

Another application example is the synthesis of titania ( $\text{TiO}_2$ ) powder in a laboratory aerosol reactor.<sup>57</sup> Here, the balance between particle aggregation and sintering leads to the formation of non-spherical particle aggregates. For an approximate shape description, their surface area is considered as a secondary characteristic property. The reactor consists of a 1.5 m long horizontal alumina pipe with an inner diameter of 31.8 mm, heated by a tubular furnace (Figure 2). Inside the reactor, titanium tetrachloride ( $\text{TiCl}_4$ ) vapor diluted by argon gas reacts with oxygen to form solid titania particles, which then grow by aggregation up to a size of about 1  $\mu\text{m}$ . A byproduct of the reaction is

chlorine. The reactor effluents are diluted by cool nitrogen to suppress further aggregation.

### 4.1 | Computational domain and boundary conditions

Gravitational settling of particles is negligible and therefore the flow in the reactor can be considered as axisymmetric. The computational domain consists of a two-dimensional section of the reactor as sketched in Figure 2. A grid spacing of about 1 mm in the radial and 2 mm in the axial direction has proven sufficient to adequately resolve the structure of the laminar flow in the reactor. For the case that is simulated here, a mixture of 2.82 L min<sup>-1</sup> argon and 0.056 L min<sup>-1</sup> oxygen carries 7.38  $\times 10^{-5}$  mol L<sup>-1</sup> of  $\text{TiCl}_4$  into the reactor. At a temperature of 1400 K within the reaction zone, this leads to a  $\text{TiCl}_4$  concentration of 1.56  $\times 10^{-5}$  mol L<sup>-1</sup>. The flow rate of the dilution nitrogen is 5 L min<sup>-1</sup>. The flow at both inlets is assumed to be fully developed and the temperatures are set to 296 K. At the wall within

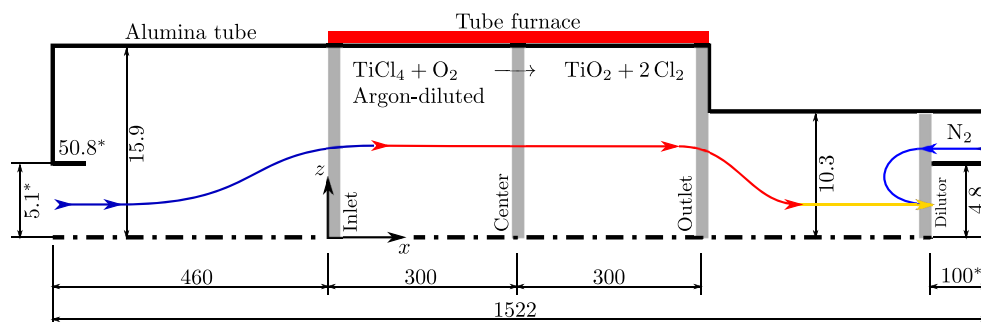


**FIGURE 2** Sketch of the aerosol reactor of Akhtar et al.<sup>57</sup> Dotted line represents the reactor axis. Dimensions are given in millimeters. Asterisks represent estimate values

the reaction zone, a measured temperature profile is applied. All other walls are assumed to be adiabatic.

## 4.2 | Key modeling aspects

For the conditions in the reactor, the stable nucleus size is smaller than the size of a single titania monomer, such that chemical reaction and nucleation cannot be distinguished.<sup>58</sup> A one-step, first-order, irreversible reaction scheme is applied to model the nucleation source term. Following Pratsinis et al.,<sup>59</sup> the mass transfer rate to be used in Equation (11) is calculated using the Arrhenius expression

$$\dot{m}_{dc} = 8.29 \times 10^4 s^{-1} e^{(-10680K/T_c)} C_{TiCl_4} M_{TiCl_4}, \quad (43)$$

where  $T_c$  is the gas temperature,  $C_{TiCl_4}$  the concentration of  $TiCl_4$  and  $M_{TiCl_4}$  its molar mass.

The particles grow by aggregation resulting from collisions due to their Brownian motion. Here, the kernel of Dahneke<sup>60</sup> is applied to model the aggregation frequency, which covers both the free molecular regime, where particle motion has a molecular character, and the continuum regime, where particle collisions are limited by diffusion. The regime in which the reactor operates depends on the ratio between the mean free path of the gas and the particle size. The former is calculated by

$$\lambda = \frac{k_B T_c}{\sqrt{2} p \sigma^2}, \quad (44)$$

where  $k_B$  is the Boltzmann constant and  $\sigma$  a parameter of the Lennard-Jones model, which evaluates to 0.34 nm for argon.<sup>61</sup> In the free molecular regime, where the particles are significantly smaller than the mean free path, the aggregation frequency is determined from

$$\tilde{C}_{fm,jj} = \left( \frac{3k_B T_c}{\rho_d} \right)^{1/2} \left( \frac{1}{d_i^3} + \frac{1}{d_j^3} \right)^{1/2} (d_i + d_j)^2. \quad (45)$$

In the continuum and near-continuum regime where the particle size is comparable to or larger than the mean free path, the aggregation frequency is given by

$$\tilde{C}_{co,jj} = \frac{8k_B T_c}{3\mu_c} \left( \frac{C_{c_i}}{d_i} + \frac{C_{c_j}}{d_j} \right) (d_i + d_j), \quad (46)$$

wherein  $\mu_c$  is the dynamic viscosity of the gas phase and

$$C_{c_i} = 1 + \frac{\lambda}{d_i} \left( 2.514 + 0.8e^{-0.55d_i/\lambda} \right) \quad (47)$$

a slip correction coefficient as proposed by Cunningham<sup>62</sup> with parameters determined by Davis,<sup>63</sup> which accounts for the reduced drag in the near-continuum regime. Written in the form proposed by Otto et al.,<sup>64</sup> Equations (45) and (46) are blended into

$$\tilde{C}_{ij} = \tilde{C}_{co,jj} \frac{1 + Kn_D}{1 + 2Kn_D + 2Kn_D^2}, \quad (48)$$

wherein

$$Kn_D = \frac{1}{2} \frac{\tilde{C}_{co,jj}}{\tilde{C}_{fm,jj}}. \quad (49)$$

The shape of the particle aggregates is determined by the characteristic time for sintering, that is, the time which is required for colliding particles to coalesce with each other. If sintering is slow compared to the process of aggregation, the resulting particle aggregates are non-spherical and have a larger collision cross section, which manifests itself in an increased aggregation frequency. Following the work of Kruis et al.,<sup>65</sup> the aggregates are assumed to have a fractal-like morphology and the diameters in Equations (45) and (46) are substituted by an approximate collision diameter  $d_c$  that is related to the aggregate volume through a power law:

$$d_c = d_{p_i} \left( \frac{v_i}{v_{p_i}} \right)^{1/D_f} = d_{p_i} (n_{p_i})^{1/D_f}. \quad (50)$$

Here,  $d_{p_i}$ ,  $v_{p_i}$ , and  $n_{p_i}$  are the diameter, volume, and number of the primary particles forming the aggregate and  $D_f$  is a mass fractal dimension. A constant value of 1.8 is adopted for  $D_f$ , which is typical for diffusion-limited aggregation of particle clusters.<sup>66</sup> Under the assumption that the primary particles are spherical and that their size distribution in each aggregate is rather narrow, tracking the primary particle

number or the surface area of the aggregates becomes equivalent. In this work, the specific surface area

$$\kappa_i = \frac{a_i}{V_i} = \frac{6}{d_{p_i}} \quad (51)$$

is selected as a secondary characteristic aggregate property as described in Section 2.1.2. Using  $\kappa_i$ , the collision diameter of the aggregates in a size class can be calculated by

$$d_c = \frac{6}{\kappa_i} \left( \frac{V_i \kappa_i^3}{36\pi} \right)^{1/D_f} \quad (52)$$

An additional transport equation is solved for the specific surface area of each size class which states

$$\frac{\partial(\kappa_i f_i \alpha)}{\partial t} + \nabla \cdot (\kappa_i f_i \alpha \vec{u}_d) = x_i H_{\kappa_i} + x_i S_{\kappa_i} \quad (53)$$

The first term on the right hand side describes its number-weighted transfer between size classes due to aggregation. It is assembled using the corresponding terms in Equation (22), wherein  $\bar{\xi}_{2,j}$  is substituted by  $\kappa_i$ . The lumped secondary property treatment adopted in Section 3 for the particle velocity is not required here, because the solution of Equation (53) is comparatively cheap. The decrease of the specific surface due to sintering of primary particles is described with the model of Koch and Friedlander,<sup>67</sup> whereby

$$S_{\kappa_i} = -\frac{N_i}{\tau_{s_i}} (\kappa_i - \kappa_{s_i}) \quad (54)$$

Herein,  $\kappa_{s_i}$  is the specific surface area of a fully sintered, that is, spherical aggregate and

$$\tau_{s_i} = 8.3 \times 10^{24} T d_{p_i}^4 e^{(3700 \text{ K}/T)} \quad (55)$$

the characteristic sintering time according to Xiong et al.<sup>4</sup>

### 4.3 | Results and discussion

Akhtar et al.<sup>57</sup> measured the temperature profile at the wall and along the center line for different flow rates using nitrogen only, that is, under non-reacting conditions. This preliminary study is repeated here to validate the simulated temperature field. The results are presented in Figure 3A. For  $1.7 \text{ L min}^{-1}$ , the agreement with the experiment is rather good. However, for  $3.5 \text{ L min}^{-1}$  a more pronounced lag of the profile is predicted. The reason for this deviation is unclear, but Jeong et al.<sup>29</sup> who also conducted two-dimensional simulations obtained similar results. It is postulated that the experimental data simply lacks a proper compensation of thermal radiation since for the laminar conditions, the center line temperature should indeed exhibit a more pronounced lag when the flow rate is doubled. The argon flow rate for the reacting case lies in between, so the deviation is considered acceptable. The corresponding axial profiles of the vapor temperature as well as the mass fractions of the reacting species are presented in Figure 3B. Starting at about 0.2 m from the beginning of the heated section, a 0.3 m long zone exists where the conditions are nearly isothermal. The conversion of  $\text{TiCl}_4$  is completed before the beginning of the isothermal section, that is, the reaction zone extends over roughly one third of the heated zone. The amount of oxygen introduced into the reactor is over-stoichiometric and therefore the corresponding mass fraction changes only slightly.

Figure 4A shows the predicted cross-sectional average of the size distribution at different axial positions. Between beginning and center of the heated section, nucleation and aggregation occur simultaneously and a wide bimodal size distribution develops. When the chemical reaction stops, the distribution gradually becomes unimodal again. Between the end of the heated section and the dilutor, the size distribution narrows due to further growth of smaller particles near the reactor axis as well as sintering of larger aggregates near the wall. Note that the size distributions are plotted with respect to the mobility diameter  $d_m$ , which is inferred from the electrical mobility of the

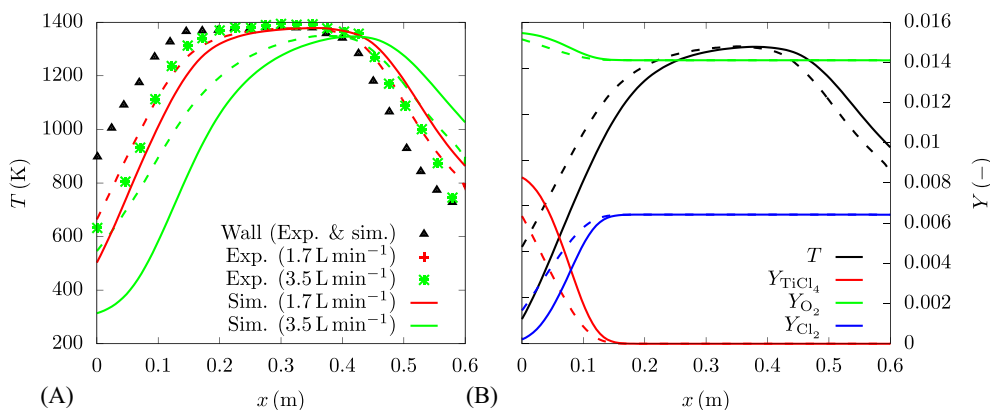


**FIGURE 3** Results for simulation of vapor synthesis of titania. (A) Temperature profiles in the reaction zone for a non-reacting case using nitrogen only with the dilutor flow rate set to  $10 \text{ L min}^{-1}$ . Note that the wall temperature profile reported by Akhtar et al.<sup>57</sup> is the same in all cases. (B) Temperature and species mass fraction profiles in the reaction zone for the reacting case. Solid lines: reactor axis. Dashed lines: cross-sectional average. Points: experiment

particles measured in a differential mobility sizer. Following Xiong et al.,<sup>4</sup> the mobility diameter is related to the surface area:

$$d_{m_i} = \sqrt{\frac{a_i}{\pi}}. \quad (56)$$

Figure 4B shows the final size distribution for three different modeling approaches in comparison to the experiment. Akhtar et al.<sup>57</sup> attempted to reproduce their experimental results by solving the population balance equation without spatial transport, that is, by using a zero-dimensional approach, assuming a mean residence time of 1.6 s and fully sintered aggregates. They predict a geometric mean diameter of 0.121  $\mu\text{m}$ , which is lower compared to the experimental result of 0.26  $\mu\text{m}$ . The calculated geometric standard deviation of 1.45 on the other hand is close to the experimentally determined value of 1.34. The predicted size distribution has a similar shape but is shifted toward smaller sizes. Akhtar et al.<sup>57</sup> suggest that diffusive losses to the reactor walls, the influence of aggregate shape and the detailed flow patterns inside the reactor should be considered for more realistic predictions. In this work, two-dimensional simulations were carried out using two different shape-modeling approaches. Assuming that the aggregates are fully sintered, the resulting geometric mean diameter lies at 0.106  $\mu\text{m}$  and the standard deviation evaluates to 1.95, which is both lower and wider than the experimental and the theoretical findings of Akhtar et al.<sup>57</sup> Considering the fractal-like shape of the aggregates leads to a geometric mean diameter of 0.18  $\mu\text{m}$  which is closer to the experiment compared to the former approaches.

Simultaneously, the size distribution is even wider with a standard deviation of 2.27. To ensure that the differences toward the predictions of Akhtar et al.<sup>57</sup> can be attributed to the shape modeling and the consideration of the flow field, a similar spatially homogeneous solution of the population balance equation with a constant temperature of 1400 K was repeated here. The results presented in Figure 4B are very close, indicating that possible differences between the numerical methods can be considered negligible.

The reason why the two-dimensional simulations generally lead to broader size distributions can be seen in Figure 5. It shows the predicted streamlines along which the particles are transported. Before the heated section, they are slightly bent as a result of the sudden expansion after the reactor inlet. Due to the contraction imposed by the outer tube of the dilutor, the particles are redirected toward the reactor axis after the heated zone. The coloring indicates the residence time, which Akhtar et al.<sup>57</sup> defined as the period for which the reactants are exposed to temperatures greater than 500 K. Clearly, the assumption of a residence time equal to 1.6 s is only valid for the particle paths near the reactor axis. Their theoretical model assumes that the aerosol is perfectly mixed and moves through the reactor as a plug. In the experiment, the flow is laminar and the associated radial velocity profile leads to a great variation of the particle residence time. This strong increase of the residence time toward the wall is what causes the wider size distribution seen in the two-dimensional simulation. What remains unclear is why the experimentally determined size distribution is narrow in comparison. A plausible reason is the design of the dilution system, which may not completely quench the aggregation process and promotes deposition of larger particles to

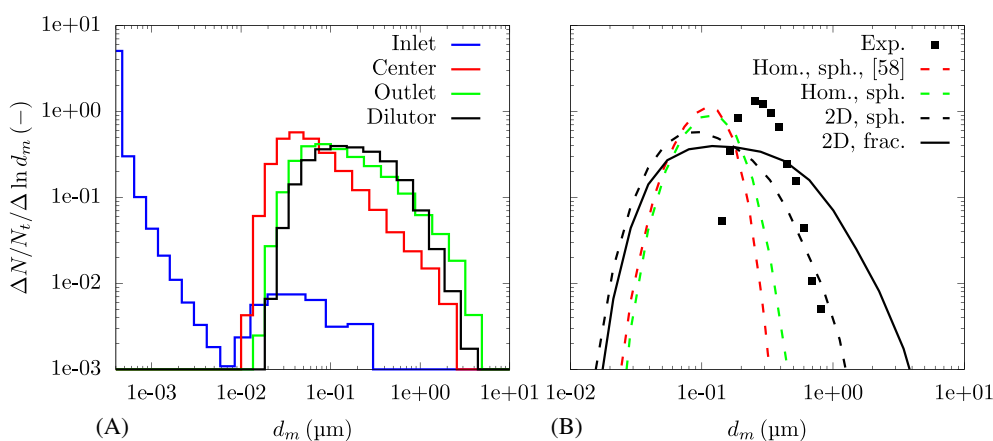


**FIGURE 4** (A) Predicted development of the size distribution along the reactor. The corresponding axial positions are evident from Figure 2. (B) Final size distribution using different modeling approaches (Hom., homogeneous population balance; sph., spherical shape; frac., fractal shape and sintering; 2D, two-dimensional simulation)

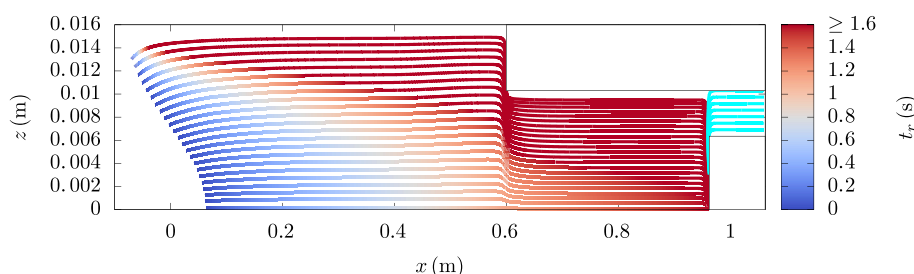


**FIGURE 5** Streamlines for  $T \geq 500$  K, colored by residence time  $t_r$

the walls through thermophoresis. Akhtar et al.<sup>57</sup> report that about 20% of the total particle mass is lost this way. Simultaneously, the temperatures in the core of the aerosol stream may still be high enough to cause further aggregation of smaller particles. A possible improvement to the design of the experiment would be to introduce the dilution nitrogen in a cross-flow configuration, that is, perpendicular to the main flow direction, in order to ensure a better mixing between the gases.

## 5 | SUMMARY AND CONCLUSIONS

A framework combining a population balance model with an Eulerian multiphase flow solver within the open source computational fluid dynamics library OpenFOAM was presented. The population balance equation is solved numerically with the method of classes based on the approach of Kumar and Ramkrishna.<sup>16</sup> As an alternative option, the approach of Liao et al.<sup>21</sup> was implemented, which allows a more efficient treatment of binary bubble breakup models with an implicitly given daughter size distribution. Both techniques support the conservation of mass and numbers while retaining flexibility in terms of discretizing the size domain. Furthermore, the population balance model was extended to account for the possibility that fluid or solid particles need to be characterized by additional properties beside the fixed representative volume. However, rather than resolving the number distribution along the secondary coordinate by tracking a two-dimensional number density function, the corresponding mean value is tracked via a separate transport equation for each size class. The generalized formulation of the framework in principle also allows to consider any number of additional properties. Exchanges between size classes through coalescence or aggregation, breakup as well as drift are taken into account by appropriate source terms. A lumped treatment was proposed, whereby consecutive sets of size classes are grouped with regard to the selected secondary property.

The application of the model was demonstrated for two fundamentally different problems. First, the cocurrent flow of air and water in a vertical pipe was investigated. It was shown that the lumped treatment of the bubble velocity as a secondary property by means of a sensible division into velocity groups provides the required degree of freedom to model a spatial separation at the control-volume level. In the second case, the gas-phase synthesis of titania powder by titanium tetrachloride oxidation in the tubular hot wall reactor of Akhtar et al.<sup>57</sup> was simulated. The agreement with the experiment is improved when the non-spherical shape of the aggregates is taken into account through tracking the specific aggregate surface area as a secondary property for each size class.

The framework developed here was integrated into the OpenFOAM Foundation release, along with several submodels, a postprocessing utility as well as verification and tutorial cases. For the simulation of the bubbly flow case, additional source code is required which is provided by Schlegel et al.<sup>68</sup> All case setups created in the scope of this work are made available by Hänsch et al.<sup>69</sup>

## ACKNOWLEDGMENTS

This work was partly supported by the Helmholtz European Partnering Program in the project “Crossing borders and scales (Crossing).” Furthermore, the authors would like to thank Henry G. Weller, CFD Direct Ltd, United Kingdom, for comments and discussions around the implementation in OpenFOAM. Open Access funding enabled and organized by Projekt DEAL.

## AUTHOR CONTRIBUTIONS

**Ronald Lehnigk:** Conceptualization (lead); data curation (lead); formal analysis (lead); investigation (lead); methodology (lead); software (lead); validation (lead); visualization (lead); writing – original draft (lead); writing – review and editing (lead). **Will Bainbridge:** Software (supporting); writing – review and editing (equal). **Yixiang Liao:** Methodology (equal); software (supporting); validation (equal); writing – review and editing (equal). **Dirk Lucas:** Conceptualization (equal); funding acquisition (equal); project administration (equal); resources (lead); supervision (equal); writing – review and editing (equal). **Timo Niemi:** Methodology (equal); software (equal); validation (equal); writing – review and editing (equal). **Juho Peltola:** Funding acquisition (supporting); software (supporting); writing – review and editing (equal). **Fabian Schlegel:** Project administration (lead); software (equal); supervision (lead); writing – review and editing (lead).

## DATA AVAILABILITY STATEMENT

The software generated during this study is openly available on Github at <https://github.com/OpenFOAM/OpenFOAM-dev>. The simulation setups and additional software can be retrieved from the Rossendorf Data Repository (Rodare) at <https://doi.org/10.14278/rodare.1049> and <https://doi.org/10.14278/rodare.1048>.

## ORCID

Ronald Lehnigk  <https://orcid.org/0000-0002-5408-7370>

Yixiang Liao  <https://orcid.org/0000-0002-1277-3938>

Dirk Lucas  <https://orcid.org/0000-0003-0463-2278>

Fabian Schlegel  <https://orcid.org/0000-0003-3824-9568>

## REFERENCES

- Lucas D, Krepper E, Prasser HM. Prediction of radial gas profiles in vertical pipe flow on the basis of bubble size distribution. *Int J Therm Sci*. 2001;40:217-225. [https://doi.org/10.1016/S1290-0729\(00\)01211-4](https://doi.org/10.1016/S1290-0729(00)01211-4)
- Tomiya A, Tamai H, Zun I, Hosokawa S. Transverse migration of single bubbles in simple shear flows. *Chem Eng Sci*. 2002;57:1849-1858. [https://doi.org/10.1016/S0009-2509\(02\)00085-4](https://doi.org/10.1016/S0009-2509(02)00085-4)
- Pratsinis SE. Flame aerosol synthesis of ceramic powders. *Prog Energy Combust Sci*. 1998;24:197-219. [https://doi.org/10.1016/S0360-1285\(97\)00028-2](https://doi.org/10.1016/S0360-1285(97)00028-2)
- Xiong Y, Akhtar MK, Pratsinis SE. Formation of agglomerate particles by coagulation and sintering—part II. The evolution of the morphology of aerosol-made titania, silica and silica-doped titania powders. *J Aerosol Sci*. 1993;24:301-313. [https://doi.org/10.1016/0021-8502\(93\)90004-S](https://doi.org/10.1016/0021-8502(93)90004-S)
- Hulburt HM, Katz S. Some problems in particle technology: a statistical mechanical formulation. *Chem Eng Sci*. 1964;19:555-574. [https://doi.org/10.1016/0009-2509\(64\)85047-8](https://doi.org/10.1016/0009-2509(64)85047-8)



6. Randolph AD. A population balance for countable entities. *Can J Chem Eng.* 1964;42:280-281. <https://doi.org/10.1002/cjce.5450420612>
7. Lehr F, Millies M, Mewes D. Bubble-size distributions and flow fields in bubble-columns. *AIChE J.* 2002;48:2426-2443. <https://doi.org/10.1002/aic.690481103>
8. Bhole MR, Joshi JB, Ramkrishna D. CFD simulation of bubble columns incorporating population balance modeling. *Chem Eng Sci.* 2008;63:2267-2282. <https://doi.org/10.1016/j.ces.2008.01.013>
9. Passalacqua A, Laurent F, Madadi-Kandjani E, Heylmun JC, Fox RO. An open-source quadrature-based population balance solver for OpenFOAM. *Chem Eng Sci.* 2018;176:306-318. <https://doi.org/10.1016/j.ces.2017.10.043>
10. Marchisio DL, Vigil RD, Fox RO. Implementation of the quadrature method of moments in CFD codes for aggregation-breakage problems. *Chem Eng Sci.* 2003;58:3337-3351. [https://doi.org/10.1016/S0009-2509\(03\)00211-2](https://doi.org/10.1016/S0009-2509(03)00211-2)
11. Marchisio DL, Fox RO. Solution of population balance equations using the direct quadrature method of moments. *J Aerosol Sci.* 2005;36:43-73. <https://doi.org/10.1016/j.jaerosci.2004.07.009>
12. Yuan C, Laurent F, Fox RO. An extended quadrature method of moments for population balance equations. *J Aerosol Sci.* 2012;51:1-23. <https://doi.org/10.1016/j.jaerosci.2012.04.003>
13. Yuan C, Fox RO. Conditional quadrature method of moments for kinetic equations. *J Comput Phys.* 2011;230:8216-8246. <https://doi.org/10.1016/j.jcp.2011.07.020>
14. Zucca A, Marchisio DL, Vanni M, Barresi AA. Validation of bivariate DQMOM for nanoparticle processes simulation. *AIChE J.* 2007;53:918-931. <https://doi.org/10.1002/aic.11125>
15. Buffo A, Marchisio DL, Vanni M, Renze P. Simulation of polydisperse multiphase systems using population balances and example application to bubbly flows. *Chem Eng Res Des.* 2013;91:1859-1875. <https://doi.org/10.1016/j.cherd.2013.06.021>
16. Kumar S, Ramkrishna D. On the solution of population balance equations by discretization-I. A fixed pivot technique. *Chem Eng Sci.* 1996;51:1311-1332. [https://doi.org/10.1016/0009-2509\(96\)88489-2](https://doi.org/10.1016/0009-2509(96)88489-2)
17. Chen P, Dudukovic MP, Sanyal J. Three-dimensional simulation of bubble column flows with bubble coalescence and breakup. *AIChE J.* 2005;51:696-712. <https://doi.org/10.1002/aic.10381>
18. Bannari R, Kerdouss F, Selma B, Bannari A, Proulx P. Three-dimensional mathematical modeling of dispersed two-phase flow using class method of population balance in bubble columns. *Comput Chem Eng.* 2008;32:3224-3237. <https://doi.org/10.1016/j.compchemeng.2008.05.016>
19. Selma B, Bannari R, Proulx P. Simulation of bubbly flows: comparison between direct quadrature method of moments (DQMOM) and method of classes (CM). *Chem Eng Sci.* 2010;65:1925-1941. <https://doi.org/10.1016/j.ces.2009.11.018>
20. Shang X, Ng BF, Wan MP, Ding S. Investigation of CFD-PBM simulations based on fixed pivot method: influence of the moment closure. *Chem Eng J.* 2020;382:122882. <https://doi.org/10.1016/j.cej.2019.122882>
21. Liao Y, Oertel R, Kriebitzsch S, Schlegel F, Lucas D. A discrete population balance equation for binary breakage. *Int J Numer Methods Fluids.* 2018;87:202-215. <https://doi.org/10.1002/fld.4491>
22. Lo S. Modelling of bubble breakup and coalescence with the MUSIG model. AEA Technical Report; 1998.
23. Krepper E, Lucas D, Prasser HM. On the modelling of bubbly flow in vertical pipes. *Nucl Eng Des.* 2005;235:597-611. <https://doi.org/10.1016/j.nucengdes.2004.09.006>
24. Cheung SCP, Yeoh GH, Tu JY. On the numerical study of isothermal vertical bubbly flow using two population balance approaches. *Chem Eng Sci.* 2007;62:4659-4674. <https://doi.org/10.1016/j.ces.2007.05.030>
25. Frank T, Zwart PJ, Krepper E, Prasser HM, Lucas D. Validation of CFD models for mono- and polydisperse air-water two-phase flows in pipes. *Nucl Eng Des.* 2008;238:647-659. <https://doi.org/10.1016/j.nucengdes.2007.02.056>
26. Liao Y, Rzehak R, Lucas D, Krepper E. Baseline closure model for dispersed bubbly flow: bubble coalescence and breakup. *Chem Eng Sci.* 2015;122:336-349. <https://doi.org/10.1016/j.ces.2014.09.042>
27. Olmos E, Gentric C, Vial C, Wild G, Midoux N. Numerical simulation of multiphase flow in bubble column reactors. Influence of bubble coalescence and break-up. *Chem Eng Sci.* 2001;56:6359-6365. [https://doi.org/10.1016/S0009-2509\(01\)00204-4](https://doi.org/10.1016/S0009-2509(01)00204-4)
28. Díaz ME, Iranzo Y, Cuadra D, Barbero R, Montes FJ, Galán MA. Numerical simulation of the gas-liquid flow in a laboratory scale bubble column: influence of bubble size distribution and non-drag forces. *Chem Eng J.* 2008;139:363-379. <https://doi.org/10.1016/j.cej.2007.08.015>
29. Jeong JI, Choi M. Analysis of non-spherical polydisperse particle growth in a two-dimensional tubular reactor. *J Aerosol Sci.* 2003;34:713-732. [https://doi.org/10.1016/S0021-8502\(03\)00028-4](https://doi.org/10.1016/S0021-8502(03)00028-4)
30. Krepper E, Lucas D, Frank T, Prasser HM, Zwart PJ. The inhomogeneous MUSIG model for the simulation of polydispersed flows. *Nucl Eng Des.* 2008;238:1690-1702. <https://doi.org/10.1016/j.nucengdes.2008.01.004>
31. Frank T, Zwart PJ, Shi JM, Krepper E, Lucas D & Rohde U. Inhomogeneous MUSIG model - a population balance approach for polydispersed bubbly flows. Paper presented at: Proceedings of the International Conference for Nuclear Energy for New Europe; September 5-8, 2005; Bled, Slovenia.
32. Cheng J, Li Q, Yang C, Zhang Y, Mao Z. CFD-PBE simulation of a bubble column in OpenFOAM. *Chin J Chem Eng.* 2018;26:1773-1784. <https://doi.org/10.1016/j.cjche.2017.11.012>
33. Li Q, Cheng J, Yang C, Mao ZS. CFD-PBE simulation of an airlift loop crystallizer. *Can J Chem Eng.* 2018;96:1382-1395. <https://doi.org/10.1002/cjce.23086>
34. Alopaeus V, Laakkonen M, Aittamaa J. Solution of population balances with breakage and agglomeration by high-order moment-conserving method of classes. *Chem Eng Sci.* 2006;61:6732-6752. <https://doi.org/10.1016/j.ces.2006.07.010>
35. Buffo A, Jama M, Alopaeus V. Liquid-liquid extraction in a rotating disc column: solution of 2D population balance with HMMC. *Chem Eng Res Des.* 2016;115:270-281. <https://doi.org/10.1016/j.cherd.2016.09.002>
36. Buffo A, Alopaeus V. A novel simplified multivariate PBE solution method for mass transfer problems. *Chem Eng Sci.* 2017;172:463-475. <https://doi.org/10.1016/j.ces.2017.06.036>
37. Kumar J. Numerical approximations of population balance equations in particulate systems. PhD thesis. Otto-von-Guericke-Universität Magdeburg; 2007.
38. Hounslow MJ, Ryall RL, Marshall VR. A discretized population balance for nucleation, growth, and aggregation. *AIChE J.* 1988;34:1821-1832. <https://doi.org/10.1002/aic.690341108>
39. Park SH, Rogak SN. A novel fixed-sectional model for the formation and growth of aerosol agglomerates. *J Aerosol Sci.* 2004;35:1385-1404. <https://doi.org/10.1016/j.jaerosci.2004.05.010>
40. Cheng J, Yang C, Jiang M, Li Q, Mao ZS. Simulation of antisolvent crystallization in impinging jets with coupled multiphase flow-mixing-PBE. *Chem Eng Sci.* 2017;171:500-512. <https://doi.org/10.1016/j.ces.2017.06.011>
41. Kurganov A, Tadmor E. New high-resolution central schemes for nonlinear conservation laws and convection-diffusion equations. *J Comput Phys.* 2000;160:241-282. <https://doi.org/10.1006/jcph.2000.6459>
42. Luo H, Svendsen HF. Theoretical model for drop and bubble-breakup in turbulent dispersions. *AIChE J.* 1996;42:1225-1233. <https://doi.org/10.1002/aic.690420505>
43. Hagesaether L, Jakobsen HA, Hjarbo K, Svendsen HF. A coalescence and breakup module for implementation in CFD-codes. *Comput Aided*



- Chem Eng.* 2000;8:367-372. [https://doi.org/10.1016/S1570-7946\(00\)80063-2](https://doi.org/10.1016/S1570-7946(00)80063-2)
44. Ishii M. Thermo-fluid dynamic theory of two-phase flow. NASA Sti/Recon Technical Report A; 1975;75:29657.
  45. Weller HG. Derivation, modelling and solution of the conditionally averaged two-phase flow equations. Technical report, OpenCFD Ltd; 2005.
  46. Weller HG. Bounded explicit and implicit second-order schemes for scalar transport. Technical report, OpenCFD Ltd; 2006.
  47. Chen XZ, Luo ZH, Yan WC, Lu YH, Ng IS. Three-dimensional CFD-PBM coupled model of the temperature fields in fluidized-bed polymerization reactors. *AIChE J.* 2011;57:3351-3366. <https://doi.org/10.1002/aic.12548>
  48. Dutta A, Constaes D, Heynderickx GJ. Applying the direct quadrature method of moments to improve multiphase FCC riser reactor simulation. *Chem Eng Sci.* 2012;83:93-109. <https://doi.org/10.1016/j.ces.2012.04.036>
  49. Liu B, Papadikis K, Gu S, et al. CFD modelling of particle shrinkage in a fluidized bed for biomass fast pyrolysis with quadrature method of moment. *Fuel Process Technol.* 2017;164:51-68. <https://doi.org/10.1016/j.fuproc.2017.04.012>
  50. Lucas D, Krepper E, Prasser HM. Development of co-current air-water flow in a vertical pipe. *Int J Multiph Flow.* 2005;31:1304-1328. <https://doi.org/10.1016/j.ijmultiphaseflow.2005.07.004>
  51. Rzehak R, Kriebitzsch S. Multiphase CFD-simulation of bubbly pipe flow: a code comparison. *Int J Multiph Flow.* 2015;68:135-152. <https://doi.org/10.1016/j.ijmultiphaseflow.2014.09.005>
  52. Liao Y, Ma T, Krepper E, Lucas D, Fröhlich J. Application of a novel model for bubble-induced turbulence to bubbly flows in containers and vertical pipes. *Chem Eng Sci.* 2019;202:55-69. <https://doi.org/10.1016/j.ces.2019.03.007>
  53. Menter F & Esch T Elements of industrial heat transfer predictions. Paper presented at: Proceedings of the 16th Brazilian Congress of Mechanical Engineering; November 26-30, 2001; Brazil.
  54. Ma T, Santarelli C, Ziegenhein T, Lucas D, Fröhlich J. Direct numerical simulation-based Reynolds-averaged closure for bubble-induced turbulence. *Phys Rev Fluids.* 2017;2(3):034301-1-034301-11. <https://doi.org/10.1103/PhysRevFluids.2.034301>
  55. Lucas D, Krepper E, Prasser HM. Evolution of flow patterns, gas fraction profiles and bubble size distributions in gas-liquid flows in vertical tubes. *Trans Inst Fluid-Flow Mach.* 2003;112:37-46.
  56. Zaruba A, Lucas D, Prasser HM, Höhne T. Bubble-wall interactions in a vertical gas-liquid flow: bouncing, sliding and bubble deformations. *Chem Eng Sci.* 2007;62:1591-1605. <https://doi.org/10.1016/j.ces.2006.11.044>
  57. Akhtar MK, Xiong Y, Pratsinis SE. Vapor synthesis of titania powder by titanium tetrachloride oxidation. *AIChE J.* 1991;37:1561-1570. <https://doi.org/10.1557/PROC-249-139>
  58. Xiong Y, Pratsinis SE. Gas phase production of particles in reactive turbulent flows. *J Aerosol Sci.* 1991;22:637-655. [https://doi.org/10.1016/0021-8502\(91\)90017-C](https://doi.org/10.1016/0021-8502(91)90017-C)
  59. Pratsinis SE, Bai H, Biswas P, Frenklach M, Mastrangelo SVR. Kinetics of titanium (IV) chloride oxidation. *J Am Ceram Soc.* 1990;73:2158-2162. <https://doi.org/10.1111/j.1151-2916.1990.tb05295.x>
  60. Dahneke B. Simple kinetic theory of Brownian diffusion in vapors and aerosols. *Theory of Dispersed Multiphase Flow.* Academic Press; 1983: 97-133.
  61. Reid RC, Prausnitz JM, Poling BE. *The Properties of Gases and Liquids.* New York, NY: McGraw Hill Book Co.; 1987.
  62. Cunningham E. On the velocity of steady fall of spherical particles through fluid medium. *Proc R Soc A Math Phys Eng Sci.* 1910;83:357-365.
  63. Davies CN. Definitive equations for the fluid resistance of spheres. *Proc Phys Soc.* 1945;57:259-270.
  64. Otto E, Fissan H, Park SH, Lee KW. The log-normal size distribution theory of brownian aerosol coagulation for the entire particle size range: part II—analytical solution using Dahneke's coagulation kernel. *J Aerosol Sci.* 1999;30:17-34. [https://doi.org/10.1016/S0021-8502\(98\)00038-X](https://doi.org/10.1016/S0021-8502(98)00038-X)
  65. Kruis FE, Kusters KA, Pratsinis SE, Scarlett B. A simple model for the evolution of the characteristics of aggregate particles undergoing coagulation and sintering. *Aerosol Sci Tech.* 1993;19:514-526. <https://doi.org/10.1080/02786829308959656>
  66. Schaefer DW. Fractal models and the structure of materials. *MRS Bull.* 1988;13:22-27.
  67. Koch W, Friedlander SK. The effect of particle coalescence on the surface area of a coagulating aerosol. *J Colloid Interface Sci.* 1990;140:419-427. [https://doi.org/10.1016/0021-8502\(89\)90719-2](https://doi.org/10.1016/0021-8502(89)90719-2)
  68. Schlegel F, Draw M, Evdokimov I, et al. (2021, July 1). HZDR Multiphase Addon for OpenFOAM (Version 2.0.0). Rodare. <http://doi.org/10.14278/rodare.1048>
  69. Hänsch S, Draw M, Evdokimov I, et al. (2021, July 1). HZDR Multiphase Case Collection for OpenFOAM (Version 2.0.0). Rodare. <http://doi.org/10.14278/rodare.1049>

## SUPPORTING INFORMATION

Additional supporting information may be found in the online version of the article at the publisher's website.

**How to cite this article:** Lehnigk R, Bainbridge W, Liao Y, et al.

An open-source population balance modeling framework for the simulation of polydisperse multiphase flows. *AIChE J.* 2022;68(3):e17539. doi:10.1002/aic.17539